

Optimized shapes of magnetic arrays for drug targeting applications

This content has been downloaded from IOPscience. Please scroll down to see the full text.

2016 J. Phys. D: Appl. Phys. 49 225501

(<http://iopscience.iop.org/0022-3727/49/22/225501>)

View [the table of contents for this issue](#), or go to the [journal homepage](#) for more

Download details:

IP Address: 86.153.12.9

This content was downloaded on 07/05/2016 at 21:29

Please note that [terms and conditions apply](#).

Optimized shapes of magnetic arrays for drug targeting applications

Lester C Barnsley, Dario Carugo and Eleanor Stride

Institute of Biomedical Engineering, Department of Engineering Science, University of Oxford, Old Road Campus Research Building, Oxford, OX3 7DQ, UK

E-mail: lester.barnsley@eng.ox.ac.uk

Received 22 December 2015, revised 23 March 2016

Accepted for publication 6 April 2016

Published 4 May 2016



CrossMark

Abstract

Arrays of permanent magnet elements have been utilized as light-weight, inexpensive sources for applying external magnetic fields in magnetic drug targeting applications, but they are extremely limited in the range of depths over which they can apply useful magnetic forces. In this paper, designs for optimized magnet arrays are presented, which were generated using an optimization routine to maximize the magnetic force available from an arbitrary arrangement of magnetized elements, depending on a set of design parameters including the depth of targeting (up to 50 mm from the magnet) and direction of force required. A method for assembling arrays in practice is considered, quantifying the difficulty of assembly and suggesting a means for easing this difficulty without a significant compromise to the applied field or force. Finite element simulations of *in vitro* magnetic retention experiments were run to demonstrate the capability of a subset of arrays to retain magnetic microparticles against flow. The results suggest that, depending on the choice of array, a useful proportion of particles (more than 10%) could be retained at flow velocities up to 100 mm s^{-1} or to depths as far as 50 mm from the magnet. Finally, the optimization routine was used to generate a design for a Halbach array optimized to deliver magnetic force to a depth of 50 mm inside the brain.

Keywords: magnetic drug targeting, Halbach array design, optimization, magnetic nanoparticle, permanent magnet flux source, targeted drug delivery

(Some figures may appear in colour only in the online journal)

1. Introduction

Magnetic drug targeting (MDT) has recently become a topic of interest among researchers due to its potential to localize and retain therapeutic agents efficiently in a target region, which has possible applications for the treatment of a range of diseases including cancer [1–5] and damaged blood vessels [6–8]. MDT using permanent magnets is advantageous because static magnetic fields and forces can be applied inside the body without being attenuated by tissue or posing a risk of magnetic hyperthermia [9, 10]. There are, however a number of challenges to overcome before the technique can be considered clinically viable [9, 11]. A major issue is that magnetic

fields and, hence, forces decay rapidly with distance, limiting applications to relatively shallow targets in the human body [12–14]. Additionally, the applied magnetic force must overcome the hydrodynamic drag force of blood before a useful quantity of agent can be captured and retained against the flow of the circulatory system [15–18].

MDT delivery systems usually consist of a therapeutic agent contained within a bio-compatible carrier functionalized or loaded with superparamagnetic iron oxide nanoparticles, and much work has focused on increasing the magnetic moment of these carriers [19–22]. Mesoscopic magnetic carriers (nanometres to microns) are particularly interesting because of a favourable ratio between magnetic and Stokes' drag forces allowing for improved accumulation [10], and the ability to tailor multi-modal composite carriers that may encapsulate a combination of drugs [23], can be functionalized for application-specific biochemical interactions [24, 25]

 Original content from this work may be used under the terms of the [Creative Commons Attribution 3.0 licence](https://creativecommons.org/licenses/by/3.0/). Any further distribution of this work must maintain attribution to the author(s) and the title of the work, journal citation and DOI.

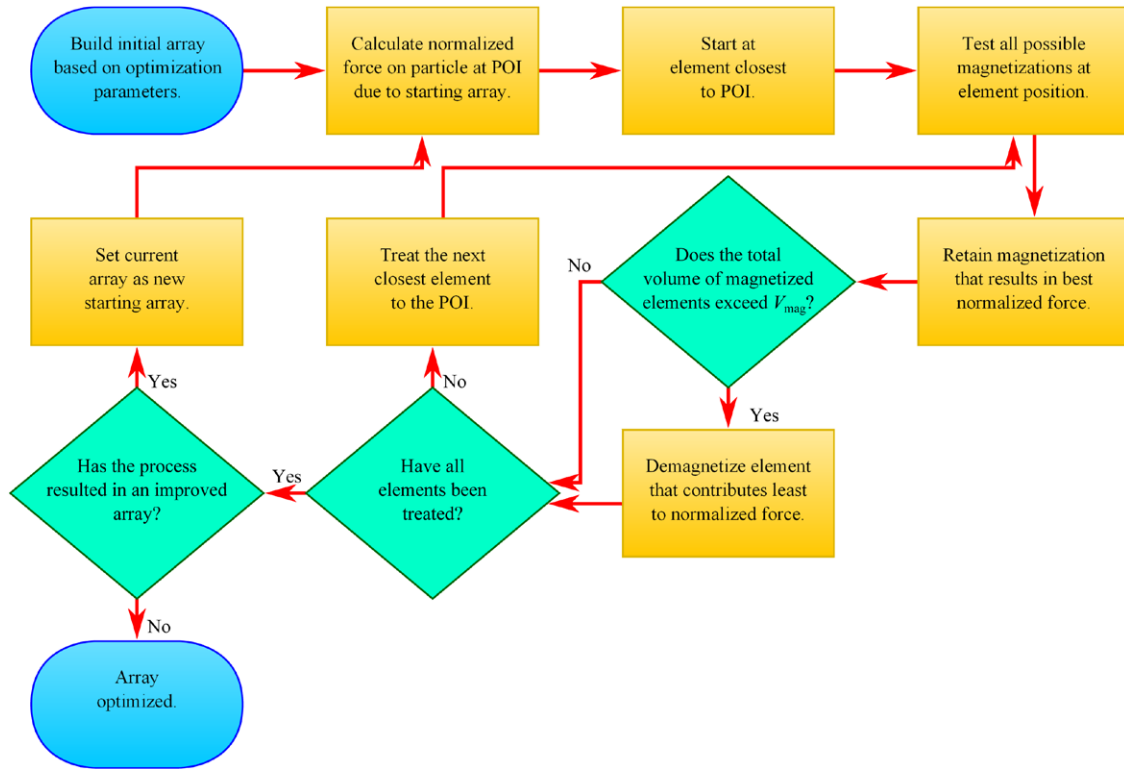


Figure 1. Flow diagram representing the routine for optimizing magnet arrays within an arbitrary parameter space.

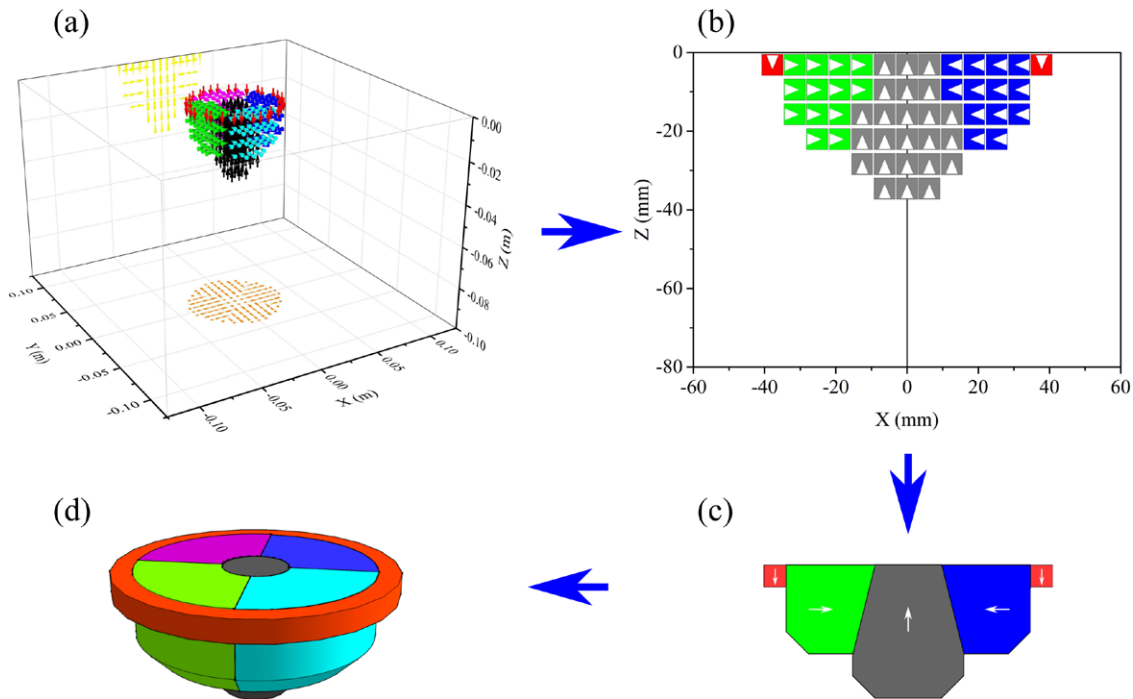


Figure 2. (a) The result of an optimization is given in terms of an arrangement of magnetization vectors which each represent the final orientation of an element in space. Vectors are colour-coded by magnetization direction. Projections onto the x - y and x - z planes are displayed on the back-planes. (b) Where the output can be approximated by a cylindrically symmetrical arrangement, the optimized configuration is projected onto a 2D plane to generate a 2D vector map of a side cross-section through the middle of the array and (c) regions with the same magnetization are merged into individual shapes. (d) The resultant magnet arrangement can then be specified in terms of a series of cylindrically symmetrical segments with different dimensions.

and are responsive to external stimuli for imaging [26] and controlled release [27, 28]. However, while it is well understood that the carrier formulation needs to be optimized for

the application [5, 11, 29, 30], there is increasing recognition that the external magnet system also needs to be tailored to the requirements and constraints of a given application,

Table 1. Parameters used in particle tracing simulations.

Symbol	Description	Value(s)	Unit
τ_p	Particle velocity response time	$\rho_p(2r_p)^2/(18\mu)$	s
μ	Fluid dynamic viscosity	8.9×10^{-4}	Pa.s
$\langle u \rangle$	Fluid flow mean velocity	2.5–250	mm s ⁻¹
m_p	Particle mass	$\rho_p(4\pi/3)r_p^3$	kg
r_p	Particle radius	5×10^{-7}	m
g	Gravity acceleration	9.8	m s ⁻²
ρ	Fluid density	1000	kg m ⁻³
ρ_p	Particle density	$(1 - \alpha)\rho_{\text{polysty}} + \alpha\rho_{\text{Fe}_3\text{O}_4}$	kg m ⁻³
ρ_{polysty}	Polystyrene density	1050	kg m ⁻³
$\rho_{\text{Fe}_3\text{O}_4}$	Fe ₃ O ₄ density	5240	kg m ⁻³
α	Volumetric ratio of Fe ₃ O ₄	0.1	
M_{NdFeB}	NdFeB magnetization	1.14×10^6	A m ⁻¹
$M_{\text{Fe}_3\text{O}_4}$	Fe ₃ O ₄ saturation magnetization	4.7×10^5	A m ⁻¹
K	Clausius–Mossotti factor	$(\mu_{r,p} - \mu_{r,f})/(\mu_{r,p} + 2\mu_{r,f})$	
$\mu_{r,p}$	Particle relative permeability	$1 + \chi$	
$\mu_{r,f}$	Fluid relative permeability	1	

accounting for the depth and physiological flow regime at the target [14, 17, 31–36].

In our previous study [37], we developed an optimization routine to determine the configuration of an assembly of inexpensive, readily available cubic permanent magnet elements offering the maximum field gradient at a given distance from the array. The aim of the present study was to significantly expand this approach to the design of magnetic arrays consisting of elements of arbitrary shape. We show that the resultant arrays are capable of generating almost two to three times as much magnetic force as arrays constructed using cubic elements for the same volume of magnetic material, depending on the optimization distance.

The difficulty of assembling arrays consisting of multiple permanent magnet segments due to the repulsive dipole forces that arise in some configurations is also considered and addressed. Designs of shapes generated using a uniform magnetization are proposed as appropriate for the soft ferromagnetic core of ‘open-pot’ electromagnets, such as that reported by Alexiou *et al* [38]. Finite element simulations of a subset of arrays are performed to demonstrate capture of magnetic particles in a range of physiologically relevant flow velocities and at depths up to 50 mm from the magnet surface. Finally, the versatility of the optimization routine is demonstrated in the form of a design of a Halbach array specifically tailored to actuate and retain magnetic particles against flow at different tissue depths inside the brain.

2. Method

2.1. Model of magnetic force

A general expression for the magnetic force, \mathbf{F} , on a single domain superparamagnetic particle with a moment of $\boldsymbol{\mu} = \mathbf{M}(\mathbf{B})V$ is given by

$$\mathbf{F} = \nabla(\boldsymbol{\mu} \cdot \mathbf{B}) = V\nabla(\mathbf{M} \cdot \mathbf{B}), \quad (1)$$

where \mathbf{M} is the magnetization of the particle, which depends on the field, V is the volume of the particle and $\mathbf{B} = \mu_0\mathbf{H}$ is the magnetic flux density, proportional to the applied field, \mathbf{H} . As the particle is superparamagnetic, it is assumed that \mathbf{M} and \mathbf{B} are parallel. The magnetization of a superparamagnetic particle can be described using a Langevin function, $L(y) = \coth(y) - 1/y$,

$$M(H) = M_s L\left(\frac{M_s V \mu_0 H}{k_B T}\right), \quad (2)$$

where M_s is the saturation magnetization of the particle, H is the applied field inside the particle and $k_B T$ is the product of the Boltzmann constant and the temperature [39–41].

The field emitted by an array consisting of an arbitrary configuration of magnetic elements was calculated by breaking the magnet into a 3-dimensional arrangement of evenly distributed point moments, following a method described previously [37]. Each moment emits a dipole field described by

$$\mathbf{B}_i(\mathbf{r}') = \frac{\mu_0}{4\pi} \left(\frac{3\mathbf{r}'(\boldsymbol{\mu}_i \cdot \mathbf{r}')}{r'^5} - \frac{\boldsymbol{\mu}_i}{r'^3} \right), \quad (3)$$

where $\boldsymbol{\mu}_i = \mathbf{M}dV$ is the point moment, \mathbf{M} is the magnetization of the permanent magnet, dV is the volume occupied by the point and \mathbf{r}' is the position vector relative to the point moment. In the optimization routine described below, the normalized magnetic force due to the field emitted by an array of magnets on a superparamagnetic particle at a position of interest (POI) was calculated. The normalized magnetic force (or force per moment) is given by

$$\frac{\mathbf{F}}{M_s V} = \frac{M}{M_s} \nabla(B) \quad (4)$$

and has units of T m⁻¹ [38]. When the particle is saturated ($M = M_s$), the normalized force is equivalent to the field gradient emitted by the array. The superparamagnetic particle considered here has the same saturation magnetization as Fe₃O₄ at room temperature ($M_s = 4.7 \times 10^5$ A m⁻¹) and a diameter of 10 nm.

The model was implemented using console applications written in the C# programming language (Microsoft Corporation, Redmond, WA, USA).

2.2. Optimization routine

An optimization routine was developed to generate designs of arbitrarily-shaped magnet arrays to deliver the maximal normalized force on a particle at the POI (\mathbf{r}_{POI}) given a series of design parameters, including the volume to be optimized, the nominal direction of normalized force ($\hat{\mathbf{F}}_{\text{nom}}$), the volume

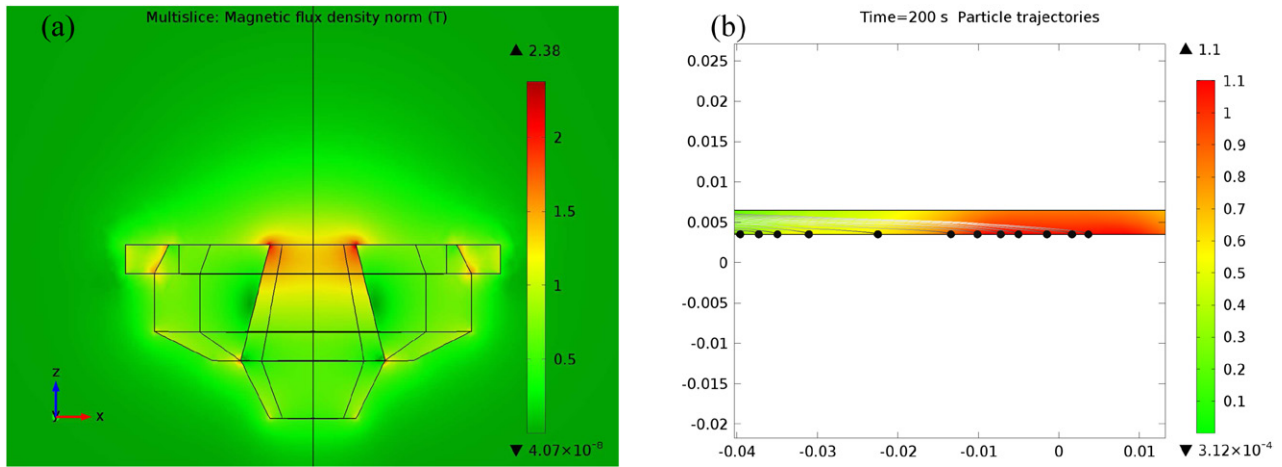


Figure 3. (a) FEM simulations were performed in COMSOL by constructing a 3D model of an orthogonally magnetized array ($z_{\text{POI}} = 20$ mm, $V = 100$ cc) following the method described in figure 2. The field inside and outside the array is calculated and mapped onto the x - z plane. (b) A laminar flow is set up in a straight, 2D channel to simulate the trajectories of magnetic microbeads (black dots) under the influence of the field generated by the array inside the channel, showing that more particles accumulate in regions where the magnetic field and force are stronger. The colour bars indicate the magnitude of the magnetic field. The direction of flow is to the right.

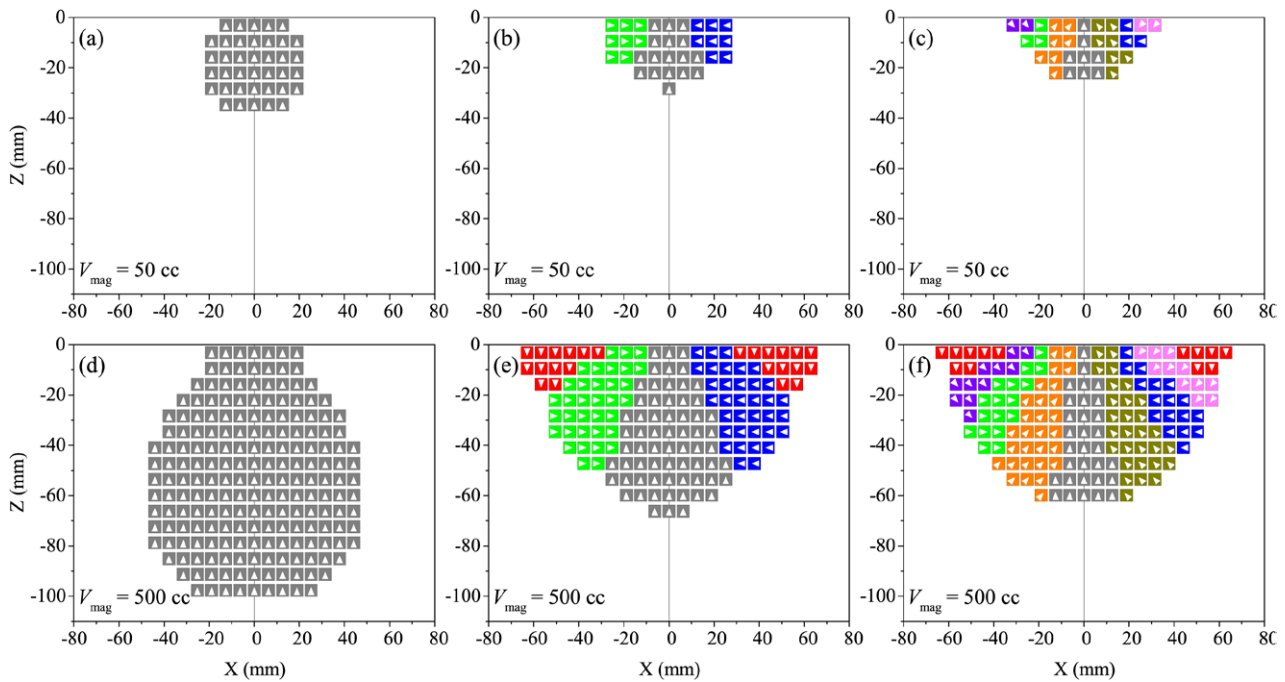


Figure 4. 2D element vector maps in the x - z plane of arrays optimized for a position of interest along the z -axis, 20 mm away from the upper face of the magnet. The first column shows designs optimized using a uniform magnetization vector set, the second column shows designs optimized with an orthogonal vector set and the third column displays optimizations using a diagonal vector set. Designs in (a)–(c) are constrained to magnet volumes of 50 cm³, while (d)–(f) are constrained to 500 cm³. Elements are colour-coded by magnetization vector.

of the magnet (V_{mag}), and the list of allowable magnetization directions contained within the array (figure 1). An initial array is constructed to occupy the volume to be optimized consisting of both magnetized and non-magnetized elements, with magnetized elements occupying the positions closest to the POI. The total volume of the magnetized elements is limited to V_{mag} at each step using a subroutine described below. The main routine then starts at the element closest to the POI and tests each allowable magnetization orientation, retaining the one that results in the best value of the optimized parameter, $\mathbf{F}(\mathbf{r}_{\text{POI}}) \cdot \hat{\mathbf{F}}_{\text{nom}}/M_s V$ generated by the whole array at the

POI. The process is then repeated for the next closest element until all elements in the array have been treated. At this point, convergence is tested by comparing the attained array to the configuration of the starting array. If the routine has changed the array and resulted in an improvement in the optimized parameter, the process is rerun using the attained array as the new starting array and again starting from the element closest to the POI until all elements have been treated. If the routine does not change the array after treating all elements and the optimized parameter cannot be improved, the array is considered optimized.

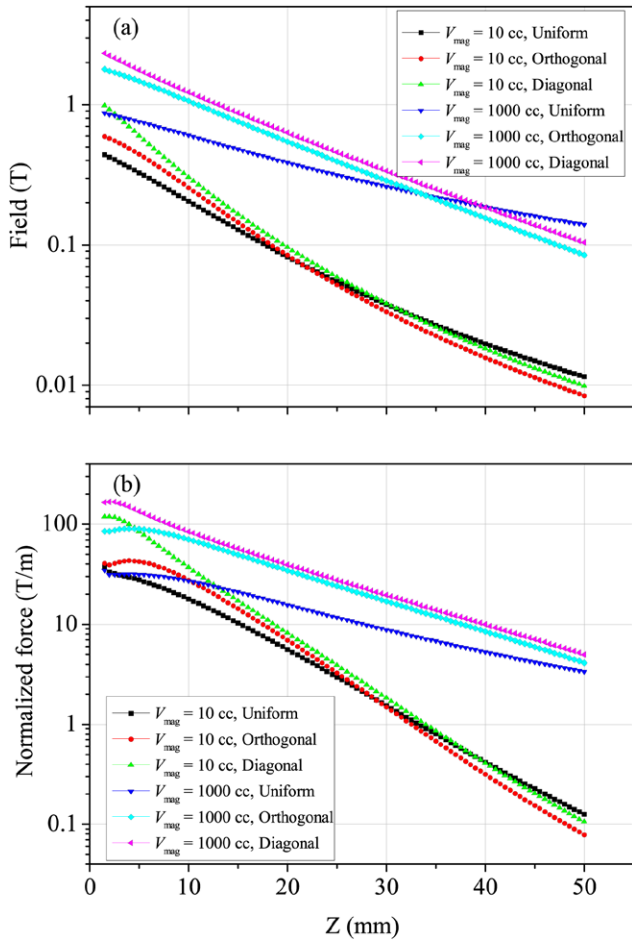


Figure 5. (a) Field profiles on a log scale along the z -axis of a subset of magnet arrays optimized with different magnet volumes. (b) Normalized force profiles on a log scale along the z -axis of the same magnet arrays.

Whenever the combined volume of all elements with a non-zero magnetization exceeds the V_{mag} parameter, a subroutine is performed in order to find and demagnetize the element that makes the least contribution to the normalized force. As the force depends on the gradient of the total field generated by the array at the POI, it cannot be assumed that this element is the element furthest from the POI. To find the element to demagnetize, each magnetized element is temporarily replaced by a non-magnetized element of the same volume and $\mathbf{F}(\mathbf{r}_{\text{POI}}) \cdot \hat{\mathbf{F}}_{\text{nom}}/M_s V$ for the remaining array is recorded. The element that makes the least difference to the optimized parameter when replaced by a non-magnetic element is demagnetized.

A collection of optimized arrays were generated by varying different parameters in the optimization routine, including the volume of the magnet, the distance between the magnet and the POI, the direction of force and the set of allowable magnetizations. Unless otherwise specified, the initial magnet array was constrained to a $0.2 \times 0.2 \times 0.1 \text{ m}^3$ optimization volume positioned directly below the x - y plane, with the POI set along the z -axis above the x - y plane. The default element density was 4 cc^{-1} . Three sets of allowable magnetization directions were investigated, within which all possible

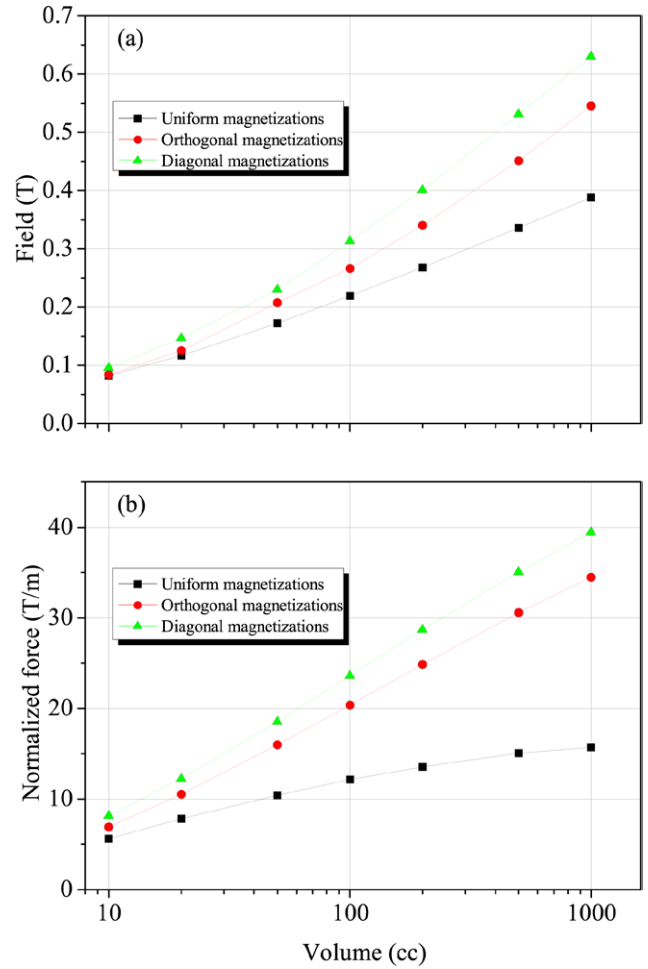


Figure 6. (a) B at the POI (along the z -axis, 20mm away from the face of the magnet) of magnet arrays optimized with different magnet volumes. (b) $F/M_s V$ for the same arrays at the same POI as a function of magnet volume.

magnetization vectors had the same magnitude as that of an N52 grade NdFeB permanent magnet ($1.14 \times 10^6 \text{ A m}^{-1}$). The first set (uniform magnetizations) contained a magnetization vector aligned with the z -axis and a zero vector (totaling two possible configurations). The second set (orthogonal magnetizations) contained six vectors pointing in the positive and negative of each orthogonal direction, along with a zero vector (seven possible configurations). The third set (diagonal magnetizations) contained all vectors in the orthogonal set, along with all possible corner and edge diagonal directions and a zero vector, totaling 27 possible magnetization configurations.

The routine returns the position and magnetization of all magnetized elements at optimization. Figure 2 shows how a resultant arrangement of magnetization vectors can be interpreted and converted into a design of constructable shapes and dimensions, particularly when the output is approximately cylindrically symmetrical (which is often the case). This is done by merging regions with the same magnetization into individual segments. The difficulty of assembling large permanent magnet segments that, in some configurations, can be strongly repulsive, must be considered [37] and is quantified here in terms of the internal magnetic potential energy, U_{int} , which is calculated by summing $-\mu_i \cdot \mathbf{B}_{\text{int}}$ for each element,

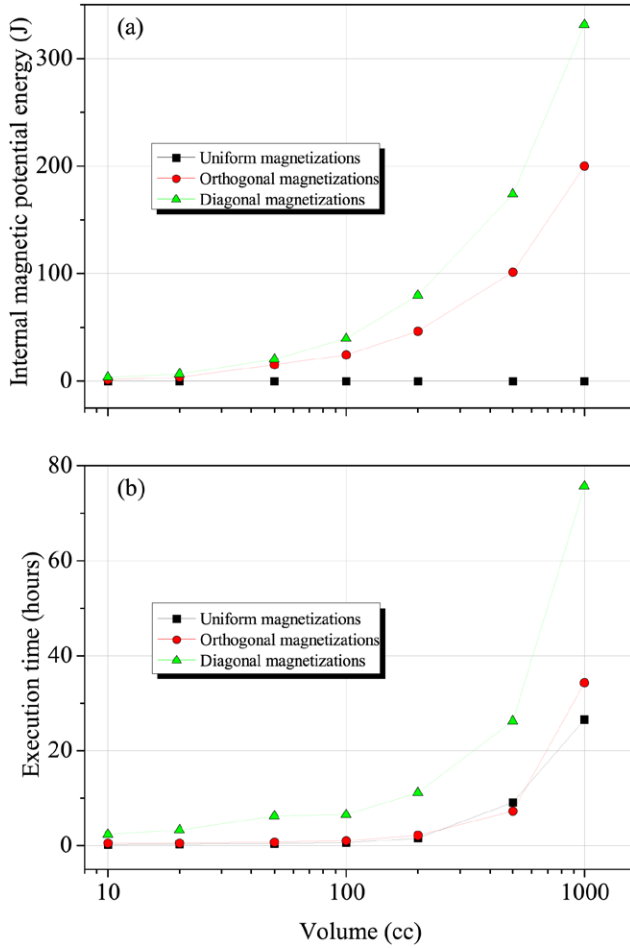


Figure 7. (a) Internal magnetic potential energy as a function of magnet volume, using different magnetization sets. (b) The total computation time of the optimization routine for each magnetization set as a function of magnet volume.

where \mathbf{B}_{int} is the field generated at the dipole position by the array without the merged magnet segment containing the element. Larger values of U_{int} are interpreted as arrays that are more difficult to assemble.

2.3. Finite element simulations

Finite element modeling was performed using COMSOL Multiphysics 5.0 (COMSOL, Inc, Burlington, MA, USA) to assess the suitability of a subset of optimized arrays for magnetic drug targeting applications via particle tracing simulations. Particles with the same properties as magnetically loaded polystyrene microbeads were simulated in a laminar flow within a straight channel primed with water flowing above the magnet in the x -direction. Capture efficiency was determined by quantifying the proportion of particles that accumulated in the region above the magnet after a simulation time of 200 s. The field emitted by a given array was calculated using the ‘magnetostatics, no currents’ interface of the ‘AC/DC module’ after constructing the geometry of the array in a 3D model following the method described for figure 2. The capture efficiency and microbead accumulation was then approximated to first-order [42] in a simplified 2D geometry

by first modeling the flow profile in a 3 mm wide channel using the ‘laminar flow’ interface of the ‘CFD module’ (setting a no-slip boundary condition at the wall and zero outlet pressure), and then using the ‘particle tracing module’ to solve the trajectories of particles in flow under the influence of a drag force, gravity and a magnetophoretic force described by the following three equations respectively:

$$\mathbf{F}_D = \left(\frac{1}{\tau_p} \right) m_p (\mathbf{u} - \mathbf{v}) \quad (5a)$$

$$\mathbf{F}_g = m_p \mathbf{g} \frac{(\rho_p - \rho)}{\rho} \quad (5b)$$

$$\mathbf{F}_M = 2\pi r_p^3 \mu_0 \mu_{r,p} K \nabla \mathbf{H}^2, \quad (5c)$$

where the various parameters are given in table 1. The field in (5c) was taken as an interpolated function of the solution to the 3D array model in the x - z plane (figure 3). The magnetic permeability of microbeads, $\mu_{r,p}$ was set to $1 + \chi$, where $\chi = M(H)/H$ is the magnetic susceptibility, and $M(H)$ is described using (2) and assuming an effective superparamagnetic cluster diameter of 10 nm to account for the fact that particles approach magnetic saturation when exposed to the particularly intense fields emitted at the face of an optimized array. The saturation magnetization of microbeads was set to $\alpha M_{s, \text{Fe}_3\text{O}_4}$, where α is the volumetric ratio of superparamagnetic Fe_3O_4 in microbeads. The density of particles was given by $\rho_p = (1 - \alpha)\rho_{\text{polysty}} + \alpha\rho_{\text{Fe}_3\text{O}_4}$.

3. Results and discussion

3.1. Volume-dependent optimizations

Optimizations were performed to generate magnet designs of different volumes between 10 and 1000 cc, using one of the three magnetization vector sets described in section 2.2, with the POI set at 20 mm along the z -axis and $\hat{\mathbf{F}}_{\text{nom}}$ directed towards the magnet (in the negative z direction). Figure 4 shows 2D element maps of a subset of optimized designs with V_{mag} constrained to 50 or 500 cc. Using a larger magnetization vector set results in arrays that are more tightly confined closer to the POI. Typically, uniform arrangements have tapered tips on the ‘front’ face of the magnet (closer to the POI), causing the field to decay more rapidly in the region close to the POI (increasing the $|\nabla(B)|$ component of (4)). This isn’t the case for the overall Halbach arrangements (consisting of orthogonal and diagonal magnetization sets), but the central magnet segment ($\mathbf{M} = M_z \hat{\mathbf{k}}$) is typically shaped in a similar way. When V_{mag} is large, the Halbach arrangements acquire a ring shaped segment around the upper surface that is uniformly magnetized in the $-\mathbf{M}_z \hat{\mathbf{k}}$ direction. In most of the Halbach designs, following the magnetization in a straight line along the diameter of the upper surface reveals a linear Halbach arrangement, with the elements magnetized to redirect the density of flux lines through the central axis of the design.

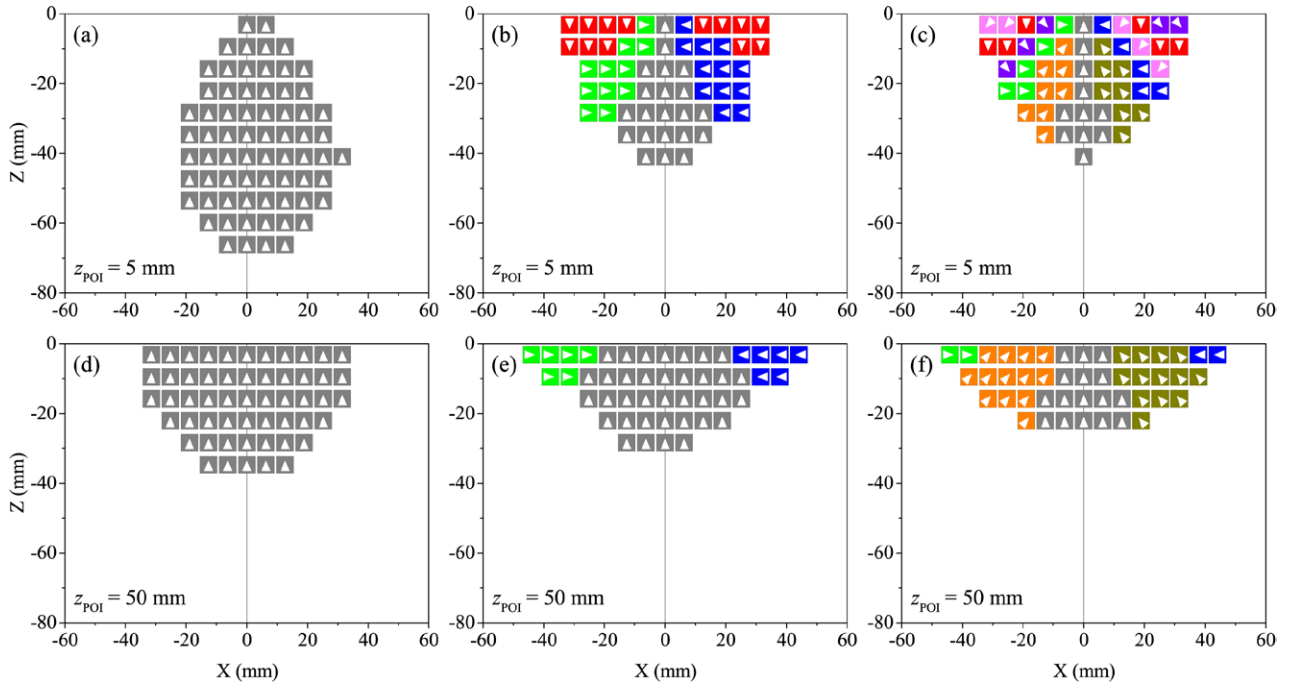


Figure 8. 2D vector maps in the x - z plane of arrays optimized for different positions of interest along the z -axis, with the magnet volume constrained to 100 cc. Arrays in the first column are uniformly magnetized, in the second column are orthogonally magnetized and in the third column are diagonally magnetized. The position of interest for designs in (a)–(c) is 5 mm from the upper surface of the magnet and, in (d)–(f) it is 50 mm from the magnet.

Figure 5 shows the dependence of the magnitude of B and $F/M_s V$ on position along the z -axis for a set of arrays with magnet volumes of 10 and 1000 cc. In each case, past a certain distance (usually about 15 mm) the field and force profiles decay approximately exponentially with distance (straight on a lin-log graph), highlighting the difficulty of applying useful magnetic forces over a long spatial range. The diagonal arrangements are able to exert significant normalized forces very close to the face of the magnet, exceeding 100 T m^{-1} , even for the 10 cc magnet, but the uniform shapes tend to perform better at long range, with the 10 and 1000 cc uniform magnet applying greater fields at $z = 50 \text{ mm}$ than Halbach arrangements of the same volume and not decaying as quickly in normalized force. Over the entire displayed range, the diagonal Halbach arrangements are superior to orthogonal designs with the same volume.

The effect of changing magnet volume on the field and force generated at the POI is displayed in figure 6. This indicates that for each magnetization set, $B(z_{\text{POI}})$ and $F(z_{\text{POI}})/M_s V$ increase approximately logarithmically with V_{mag} and, for designs with orthogonal magnetizations, a factor of ~ 5 increase in volume is required to raise the normalized force by 10 T m^{-1} . Notably, the 100 cc orthogonal array produces a normalized force of 20.3 T m^{-1} at the POI, almost twice the force of a double layer cubic element array at the same distance (11.9 T m^{-1}) reported in reference [37], which was optimized using the same set of parameters.

The internal magnetic potential energy, shown in figure 7(a) was calculated following the method described in section 2.2 as a metric to gauge the difficulty of assembling an optimized array from individual segments of uniform magnetization. Uniformly magnetized shapes have a U_{int} of 0 J assuming they

are machined from a single piece and not assembled from smaller elements that are repulsive in certain configurations. As the number of possible magnetization vectors increases and, thus, the number of segments required to assemble an array, the internal magnetic potential energy also rises. This demonstrates the main disadvantage of designs using diagonal magnetizations; while arrays utilizing diagonal configurations tend to result in the most intense field and force values, their assembly is complicated by the fact that many of the configurations between neighbouring segments are repulsive. The potential energy density in the 1000 cc array with diagonal magnetization vectors is $3.3 \times 10^5 \text{ J m}^{-3}$.

The required computation time to execute the optimization routine for each design on a computer with an Intel(R) Core(TM) i7 processor and 8 GB RAM is shown in figure 7(b). Uniformly and orthogonally magnetized arrays with $V_{\text{mag}} \leq 100 \text{ cc}$ and an element density of 4 cc^{-1} can be optimized in under an hour. Diagonally magnetized arrays require significantly more time to optimize.

3.2. Position of interest dependent optimizations

A set of optimizations was performed with the magnet volume constrained to 100 cc and the nominal direction of force fixed towards the magnet (pull force). The position of interest was varied along the z -axis and designs were generated for each of three possible magnetization sets described previously. Figure 8 shows the resultant designs with the POI set at distances of 5 and 50 mm away from the magnet. For each magnetization set, increasing z_{POI} yields designs that are more tightly confined to the x - y plane, resulting in flatter, disc shaped volumes. When the POI is very close to the face of the

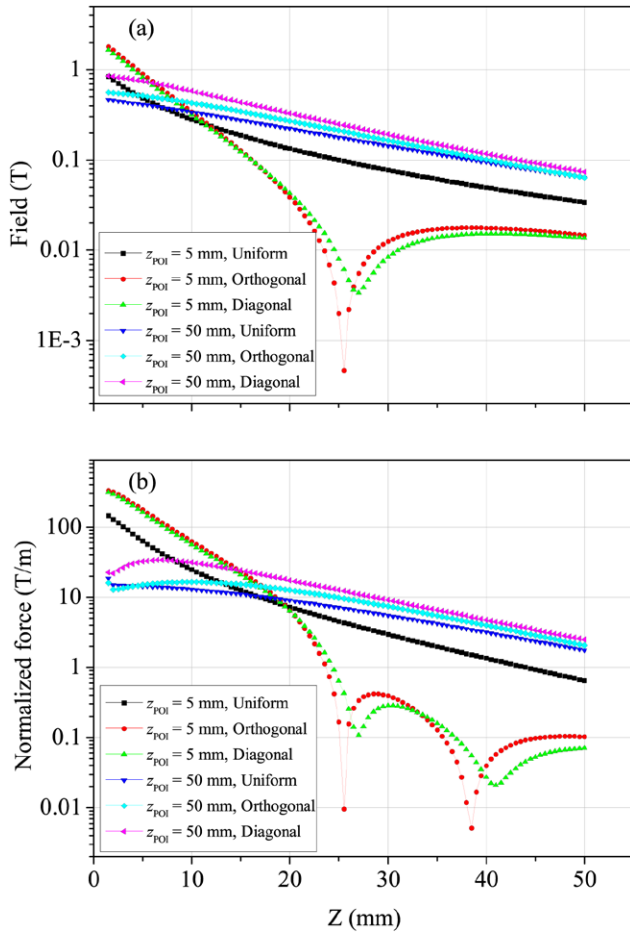


Figure 9. (a) Field profiles and (b) normalized force profiles along the z -axis of arrays shown in figure 8, optimized for either 5 or 50 mm away from the magnet face.

array (figures 8(a)–(c)), the uniformly magnetized arrays tend to exhibit the same tapered point seen in analogous designs in figure 4, while Halbach designs have more segments magnetized with a component pointing away from the POI, in order to redirect flux more efficiently through the front face of the array along the z -axis.

The relatively high proportion of elements off-axis that are magnetized away from the POI results in extremely high field and force values very close to the face of the arrays, as shown in the profiles of $|B|$ and $|F|/M_s V$ in figure 9. Both types of Halbach arrays optimized for $z_{\text{opt}} = 5$ mm are able to obtain a field of 1.6 T and a field gradient in excess of 300 T m^{-1} at short range, and are even capable of applying normalized forces greater than 100 T m^{-1} as far as 7 mm away. These field gradients are remarkable, and are more than twice as forceful as unresolved (i.e. difficult to assemble) cubic, pull arrays of the same volume reported previously (maximum $\nabla(B)$ of 139 T m^{-1}) [37], and almost three times as forceful as the corresponding resolved arrays which were determined to be easier to construct (capable of applying 124 T m^{-1}). To our knowledge, the only other magnetic systems capable of applying field gradients of several hundred T/m over millimetre length scales that have been considered for MDT are based on superconducting magnets [43, 44]. However, the

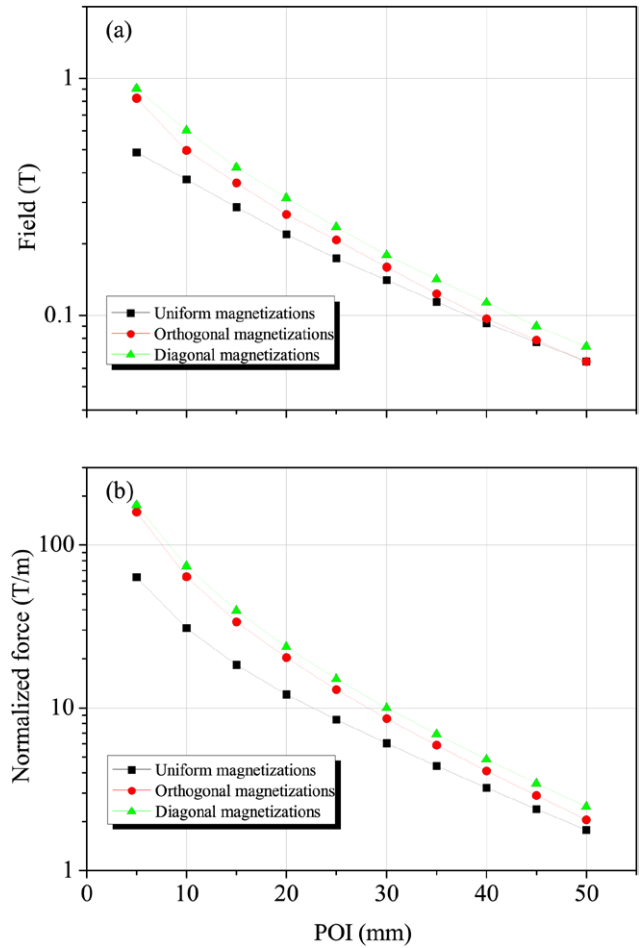


Figure 10. (a) Field and (b) normalized force of different arrays at the position of interest, as a function of the position of interest.

field profiles in figure 9(a) are not persistent and drop off fairly rapidly, with the magnitude of B exhibiting minima at about 25 mm, coinciding with a change in direction of field from positively aligned with the z -axis to negatively aligned. This results in very small push forces from the magnets in the region between ~ 25 –40 mm, between the two minima in $|F|/M_s V$ (figure 9(b)).

The fields and forces emitted by uniformly magnetized arrangements decay less rapidly as a function of distance than those emitted by orthogonal and diagonal Halbach arrays optimized for the same POI. Similarly, arrays optimized for a further POI also perform better over a longer range of distances than arrays optimized for $z_{\text{opt}} = 5$ mm. The diagonal array optimized for 50 mm is capable of delivering a normalized force greater than 10 T m^{-1} at 28.5 mm, while the field remains above 0.1 T up to 43 mm away.

Figure 10 shows how the field and normalized force vary for different arrays at the POI, as a function of POI. The behaviour of $B(z_{\text{POI}})$ highlights how the advantages of using Halbach arrays over uniform magnets diminish at long ranges, particularly for orthogonal arrangements at $z_{\text{POI}} = 50$ mm, where the improvement over the uniform design is indiscernible. Figure 10(b) shows that, while diagonal arrangements apply superior forces at all POIs, the improvement over orthogonal arrays is relatively small, particularly when

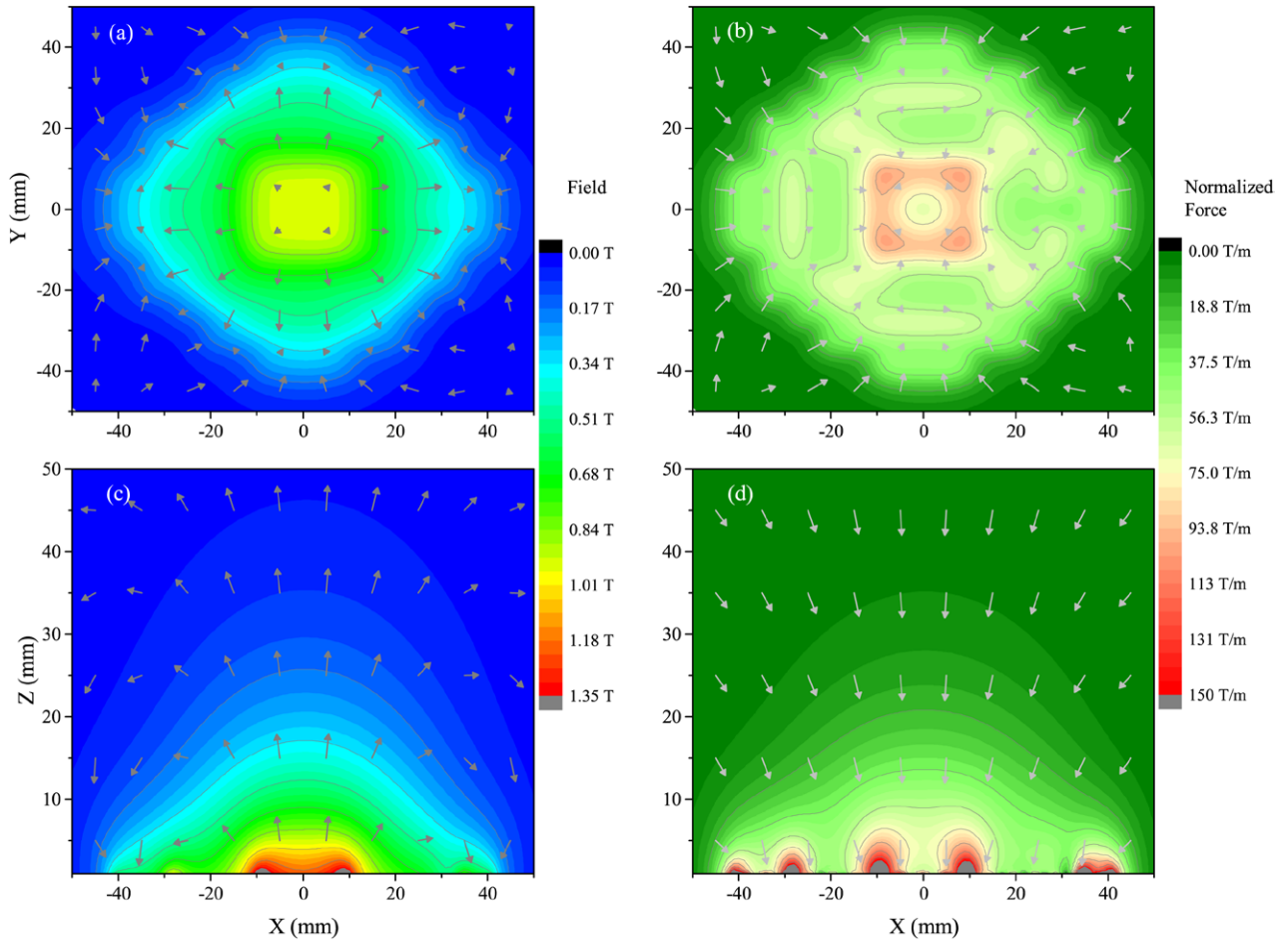


Figure 11. Simulations showing the magnitude of the (a) field and (b) normalized force in the x - y plane 5 mm above the upper surface of the orthogonal magnet design shown in figure 2 ($V_{\text{mag}} = 100$ cc, $z_{\text{POI}} = 20$ mm). (c) and (d) show the same outputs in the x - z plane above the array. The arrows indicate the direction of the field or force projected on the plane.

the POI is set close to the magnet. When $z_{\text{POI}} = 5$ mm, the performance of the diagonal arrangement is 10% better than the orthogonal array, while, for $z_{\text{POI}} = 50$ mm arrays, using a diagonal magnetization set results in a 20% greater force than the orthogonal design.

The behaviour of the field and force in a x - y and x - z plane from an orthogonal magnet design with $z_{\text{POI}} = 20$ mm is displayed in figure 11. It is noted that, while the force in the x - y plane 5 mm above the surface of the magnet is directed towards its centre axis, the strongest forces coincide with the regions where the magnetization changes on the upper surface of the design.

3.3. Direction of force dependent optimizations

The optimization routine was used to investigate how optimized designs vary with different nominal directions of force. V_{mag} was fixed to 100 cc and the POI was set at 20 mm along the z -axis, while the angle between the nominal direction of force and the negative z -axis, labeled θ , was rotated through the x - z plane (this convention was chosen so that $\theta = 0^\circ$ results in the nominal direction of force pointing toward the magnet, optimizing for a pull force, and $\theta = 180^\circ$ coincides with a nominal direction of force away from the magnet, to maximize the push force at the POI).

A subset of resultant designs consisting of uniform and orthogonal arrays is displayed in figure 12. For the uniform array with $\theta = 90^\circ$, in order to obtain a component of force in the $-x$ -direction along the z -axis, the array splits into two parts, with most of the volume of the magnet occupying the $-x$, $-z$ quadrant. When $\theta = 180^\circ$, a toroid shape results, centred around the z -axis. With this geometry, a push force results at the POI because the field close to the face of the toroid is negative along the z -axis (the cyan line in figure 13(a)). This field changes direction at a distance along the z -axis dictated by the geometry of the toroid; the transition from negative to positive field results in a push force away from the local minimum in field (figure 13(b)).

Setting $\theta = 180^\circ$ with orthogonal magnetization vectors essentially ‘inverses’ the pattern in the centre of the array, with a segment magnetized anti-parallel to z occupying the central axis, and surrounding elements magnetized to redirect flux away from this segment and into a toroid with the same magnetization and comparable dimensions to the shape generated for the uniform case.

Close to the face of the array, the field for arrays optimized with $\theta = 90^\circ$ is almost parallel to the x -axis, while the field for arrays with θ set to 180° points in the negative z -direction (figure 13(a)). However, as the distance from the

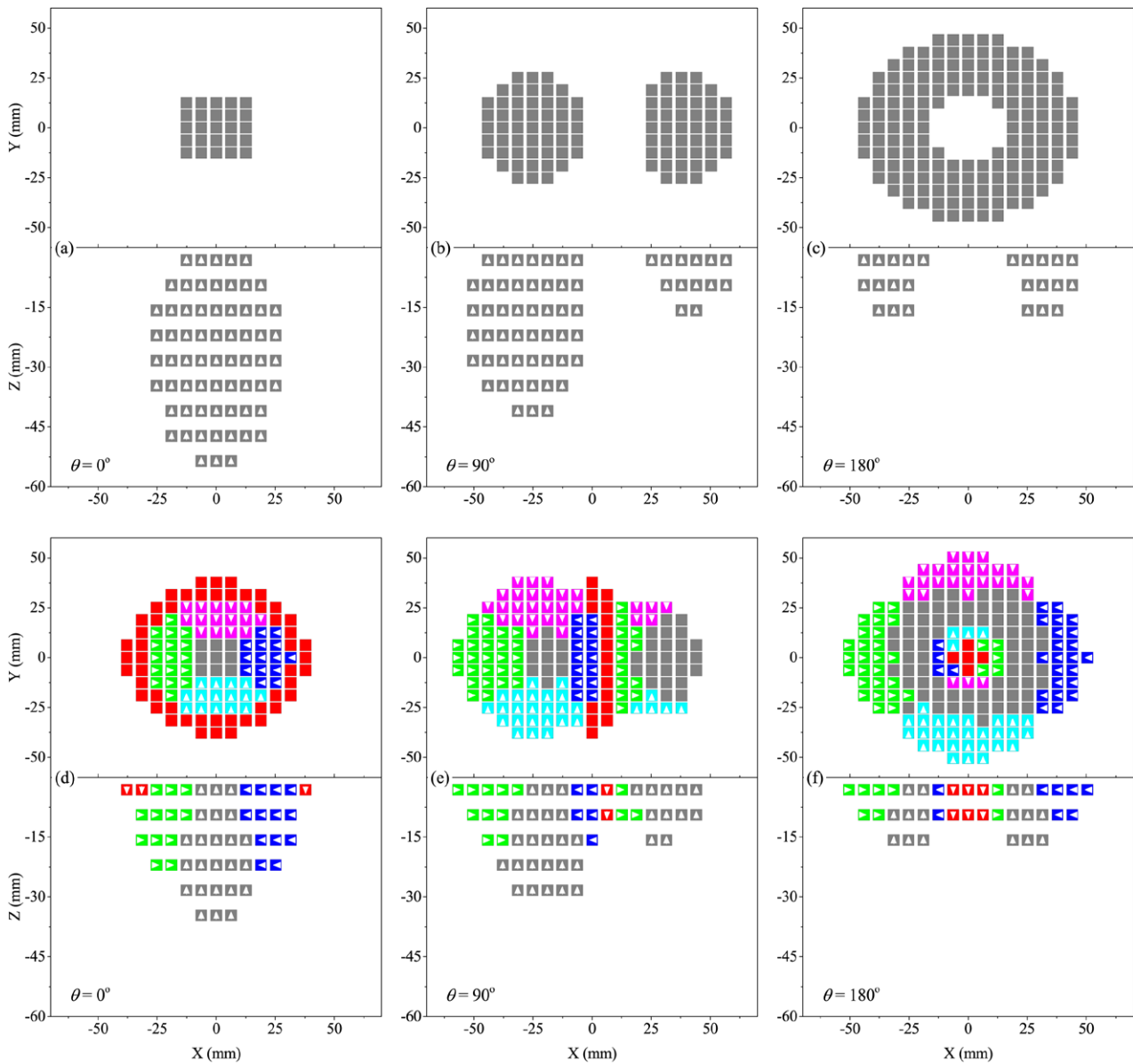


Figure 12. Designs of (a)–(c) uniformly and (d)–(f) orthogonally magnetized arrays optimized to apply forces in different directions at a distance 20 mm from the upper face of the array. Each design shows vector maps of the top x – y surface and a side x – z cross-section through the middle of the array. The first column shows designs with $\theta = 0^\circ$ (pull force), the second column shows $\theta = 90^\circ$ and the third column shows $\theta = 180^\circ$ (push force).

array increases, the field vector rotates to be more closely aligned in the z -direction, either gradually in the case of $\theta = 90^\circ$ arrays, or as a sudden transition in the case of push force arrays. Figure 13(b) shows that, even arrays optimized for $\theta = 180^\circ$ are only capable of applying a push force over a short distance of ~ 15 mm along the main axis, as seen by the range for which the force points at 180° to the $-z$ -direction (between the two minima in the magnitude of the force profiles). The range of push force is slightly greater for the uniform arrangement, but the orthogonal array gives a slightly greater force. Push force arrays can be useful for non-invasive magnetic injection when physiological flows in the region of interest are low [45, 46], but for applications where carriers need to be separated from high blood flow velocities (e.g. partially-occluded and/or injured arteries, or around the

leaky vasculature of tumours), high field gradients (more than 10 T m^{-1}) that persist over a range of several centimetres are more useful [38, 47].

The capability of arrays optimized with different θ values to deliver field or force to the POI 20 mm away is displayed in figure 14. Of interest is the fact that the angle of the relevant vectors at the POI is largely independent of the magnetization set used to generate the design, but diagonal magnetized arrays are consistently able to deliver about twice as much normalized force than the analogous uniform arrangements. However, while the diagonal magnetization set performs the best of the tested sets with all θ , the difference in performance between diagonal and orthogonal arrangements is diminished when a push force is the objective.

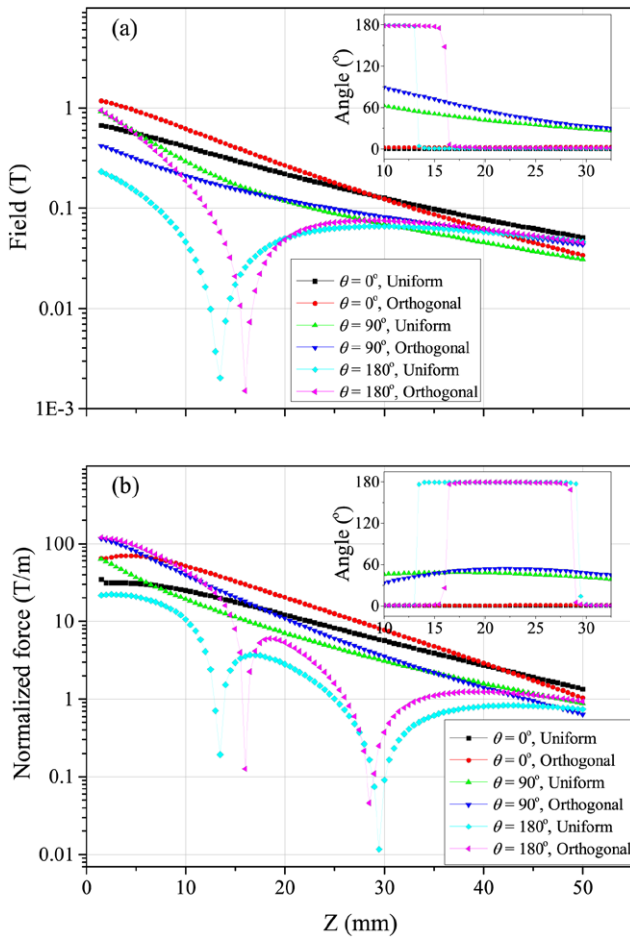


Figure 13. (a) The field along the z -axis generated by the designs of figure 12. The inset shows how the angle of this field deviates from the z -axis as a function of position. (a) The normalized force along the z -axis of the same arrays. Here, the inset shows the angle between the force vector and the $-z$ -direction.

3.4. Particle tracing simulations

Particle tracing simulations were performed using COMSOL software following the method described in section 2.3, to calculate the trajectories of magnetic microbeads in fluid flow past a subset of optimized magnet arrays. The field profiles for three orthogonal magnet arrays ($z_{POI} = 5, 20$ and 50 mm as reported in section 3.2) were calculated by assembling 3D models following the method described in figure 2. Fluid flow velocities and particle trajectories were calculated inside a 2D channel that was 3 mm wide, with the channel centre-line (corresponding to max fluid velocity) positioned at various distances, z_d between 5 and 50 mm above the upper surface of the array. As the laminar flow profiles were calculated in 2D, the velocity along the centre-line of the channel was 1.5 times the nominal, mean flow velocity, which was varied between 2.5 and 250 mm s⁻¹ (corresponding to Reynolds numbers between 8.4 and 840). The lower end of this range is of the same order as blood flow velocities in the cerebral cortex [48, 49], while the upper end of this range is comparable with those observed in tumours [50, 51].

Mesh independence was determined for the 3D model of the $z_{POI} = 50$ mm orthogonal array by using the available

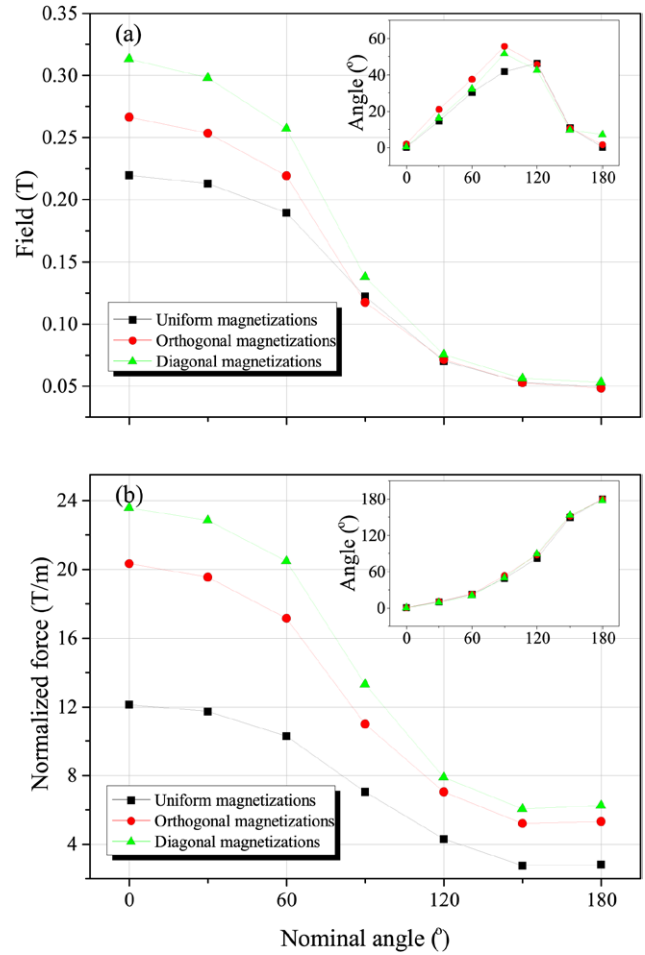


Figure 14. (a) Field and (b) normalized force of different arrays at the position of interest, as a function of θ . The insets give the angles of the vectors at the POI, as defined in figure 13.

physics-controlled meshes and increasing the mesh density until no variation was observed in the field profile along the z -axis. Figure 15(a) shows that mesh independence is obtained once the mesh density exceeds $\sim 2.14 \times 10^6$ elements m⁻³ and that the finite element calculations agreed well with the dipole model for all meshes. As calculation of magnetic field using COMSOL's interfaces was not computationally intensive on the PC described in section 3.1, the finest available physics-controlled mesh density was used for all subsequent calculations of field profiles for the other arrays. A similar procedure was followed for the 2D model by calculating the fluid velocity magnitude along the width of the channel (figure 15(b)), and mesh independence was attained for meshes with a density greater than 9.33×10^7 elements m⁻². A mesh density of 2.68×10^8 elements m⁻² was used for particle tracing simulations (containing a minimum element size of 2.08×10^{-6} m).

Figure 16 shows the capture efficiency of microparticles as a function of flow velocity using different arrays and with the channel set at different distances. In each case, the capture efficiency decays approximately as a power law with flow velocity, typically with an index of about -0.6 (closer to -0.7 when $z_d = 50$ mm). At a channel position of 5 mm, there is very little difference in the total capture efficiency of the $z_{POI} = 5$ mm and $z_{POI} = 20$ mm arrays, although there is

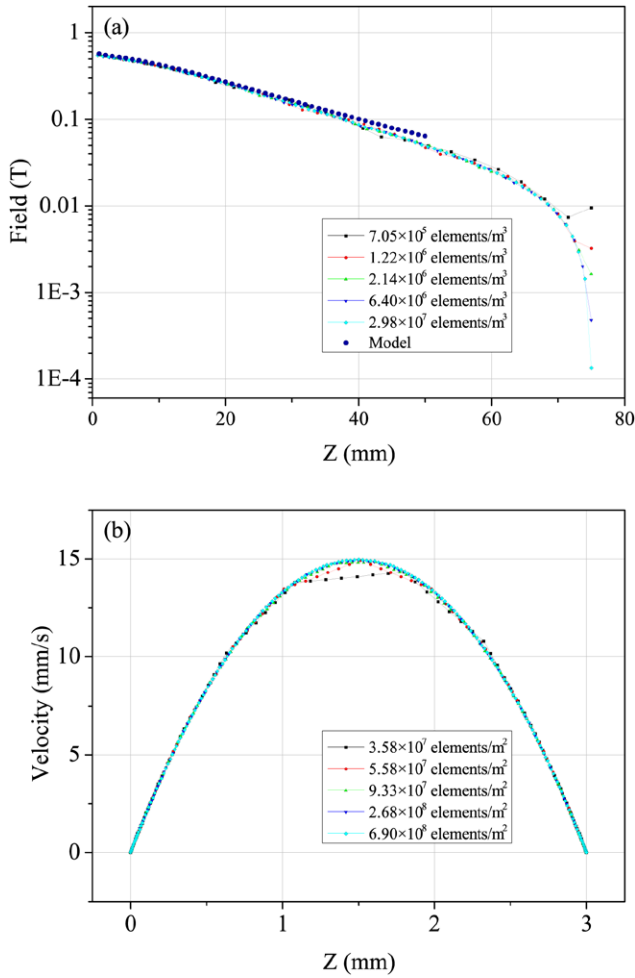


Figure 15. (a) FEM simulations in 3D of field profiles along the z -axis of an orthogonally magnetized array optimized for $z_{POI} = 50$ mm using different mesh densities, compared with predictions using the dipole model (black dots). (b) 2D simulations of the flow profile in a 3 mm diameter channel with a mean inlet flow velocity of 10 mm s^{-1} . In these simulations, mesh independence is obtained once the mesh density exceeds $9.33 \times 10^7 \text{ elements m}^{-2}$.

a difference in the distribution of captured particles along the length of the channel (figure 17(b)). At further channel distances, the $z_{POI} = 5$ mm array is vastly inferior to the other two arrays due to the fact that its applied force decays most rapidly with space, while the array that performs the best is the one that was optimized for that range. Our previous work on magnetic carriers [37, 52] has indicated that a capture efficiency of 10% is sufficient to significantly increase the acoustic response detected from retained magnetic micro-bubbles under ultrasound exposure and this would in turn be expected to generate a therapeutic effect [53]. On this basis an optimized array (i.e. $z_{POI} = z_d$) would be able to retain a diagnostically and/or therapeutically relevant number of particles in flow velocities of 100 mm s^{-1} at 5 mm, 25 mm s^{-1} at 20 mm and 2.5 mm s^{-1} at 50 mm.

The accumulation distribution was quantified by counting the relative proportion of captured microparticles that were distributed along the length of the channel above the magnet in 5 mm incremental sections. The accumulation distribution inside the channel set 5 mm above the $z_{POI} = 20$ mm array is

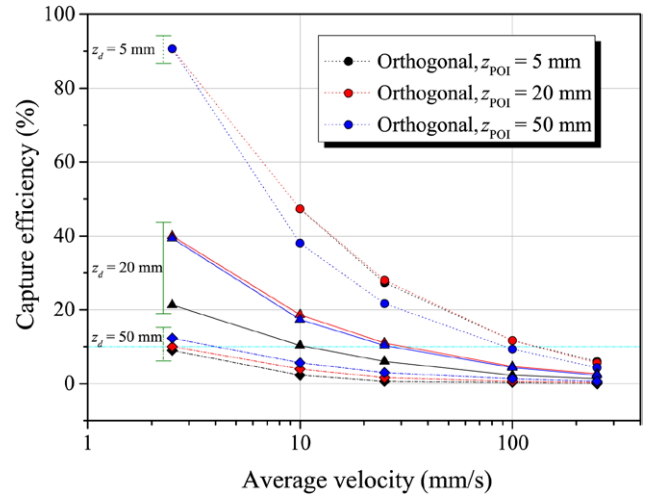


Figure 16. Capture efficiency as a function of velocity. Simulations were performed using three different orthogonally magnetized arrays, $z_{POI} = 5$ mm (black), $z_{POI} = 20$ mm (red) and $z_{POI} = 50$ mm (blue) and three different channel positions, 5 mm (dotted lines), 20 mm (solid lines) and 50 mm (dashed lines) away from the face of the magnet. The teal line indicates a useful capture efficiency.

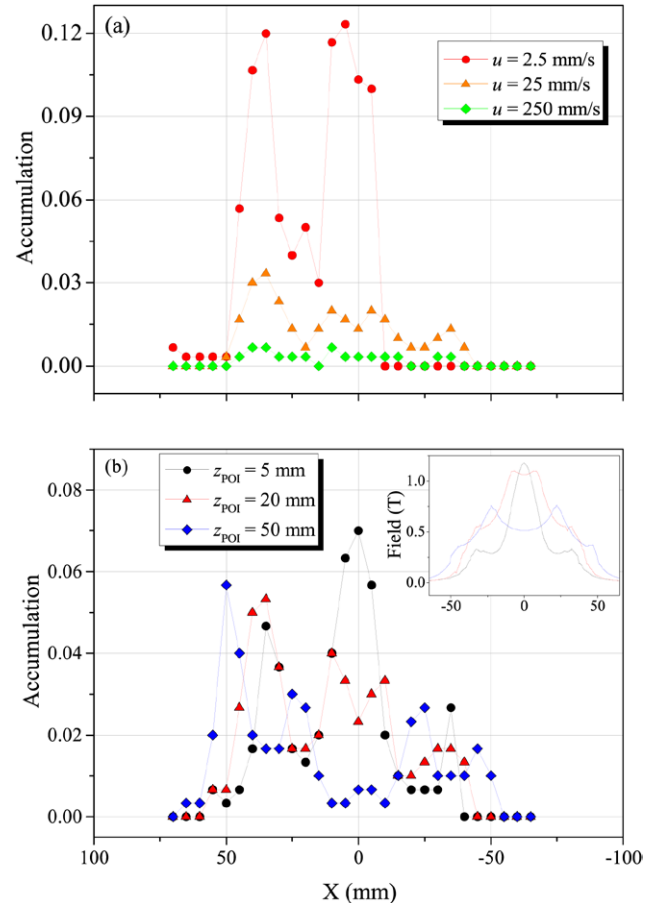


Figure 17. (a) The relative proportion of accumulated particles along the length of the channel above the magnet at different inlet flow velocities. The channel is positioned 5 mm above an orthogonal array ($z_{POI} = 20$ mm). (b) The accumulation distribution with different arrays ($z_{POI} = 5$ mm in black, $z_{POI} = 20$ mm in red, $z_{POI} = 50$ mm in blue) and u set to 10 mm s^{-1} . The inset shows how the magnitude of the field varies along the bottom of the channel for each array.

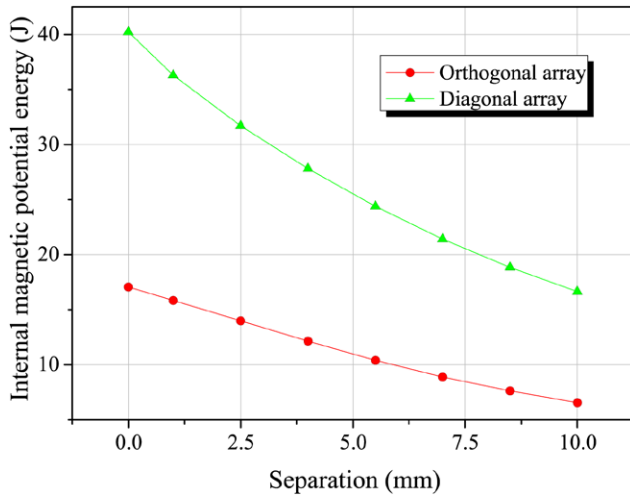


Figure 18. U_{int} versus a minimum separation distance between each segment in the designs of orthogonal and diagonal Halbach arrays initially optimized for a distance 50 mm from the magnet ($V_{\text{mag}} = 100$ cc).

displayed in figure 17(a). At all velocities, two peaks emerge, one coinciding with the z -axis, above the centre of the array, and one coinciding with the leading edge of the array, where the field profile has a local shoulder. Figure 17(b) shows how accumulation varies using the different arrays and setting the inlet velocity to 10 mm s^{-1} . At this range, the $z_{\text{POI}} = 5 \text{ mm}$ array is better able to localize more particles in the region near to the centre of the array, owing to a strong attraction to the particularly intense and narrow peak in field profile in this region along the channel (displayed in the inset). The $z_{\text{POI}} = 50 \text{ mm}$ array exhibits a local minimum in the field around this region, resulting in very few particles being directed to the target.

3.5. Consideration of assembly forces

In order to assemble Halbach arrays, the sometimes repulsive dipole forces that arise between neighbouring permanent magnet elements must be overcome. This challenge can be somewhat mitigated by separating neighbouring segments that are in repulsive configurations, but this may result in a compromise in the field and force generated by the array along the z -axis. The designs of the 100 cc orthogonally and diagonally magnetized Halbach arrays optimized for $z_{\text{POI}} = 50 \text{ mm}$ (displayed in figures 8(e) and (f)) were resimulated after introducing a minimum separation distance, d between each segment.

Figure 18 shows how introducing a gap up to 10 mm between segments can reduce the internal magnetic potential energy associated with each array, U_{int} which is used to gauge the relative difficulty of assembling a given array. Introducing a gap of 10 mm into the orthogonal array lowers U_{int} by more than 60%, compared with the same design with no gap. Our model allows us to compare this quantity to that of other arrays reported in the literature, such as a Halbach cylinder ($108 \text{ o.d.} \times 54 \text{ i.d.} \times 115 \text{ mm}^3$) assembled by Cugat *et al* [54]. Our analysis suggests this design has a U_{int} value

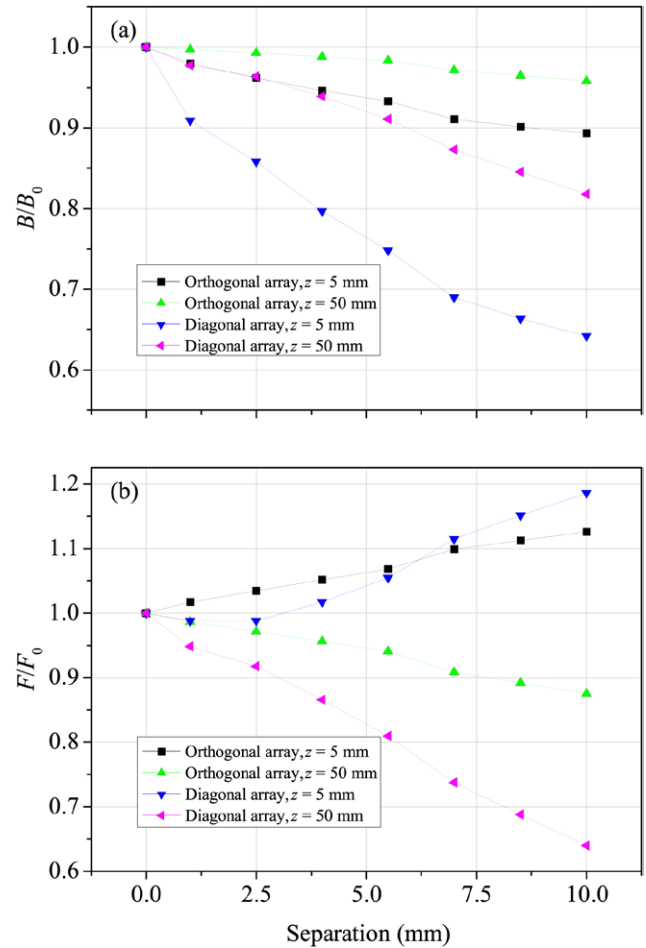


Figure 19. (a) The ratio between $B(d)$ and $B(d = 0)$ for orthogonal and diagonal designs initially optimized for $z_{\text{POI}} = 50 \text{ mm}$, calculated at 5 and 50 mm along the z -axis. (b) The ratio between $F(d)$ and $F(d = 0)$ for the same arrays at the same positions.

of 10.6 J , which is favourably comparable to the values we report for optimized orthogonal arrays with separations greater than $\sim 6 \text{ mm}$, implying that the challenges associated with assembling these designs can be overcome. The potential energy density of the orthogonal design with $d = 10 \text{ mm}$ is $6.56 \times 10^4 \text{ J m}^{-3}$.

The field, B and force, F generated by the orthogonal and diagonal arrays with different separation distances were calculated along the z -axis at positions 5 and 50 mm away from the magnets. Figure 19 shows how B/B_0 and F/F_0 vary for these two arrays at these two positions for different gap sizes, d , where B_0 and F_0 are the field and force respectively when $d = 0 \text{ mm}$. Varying d has a much greater effect on the diagonal array than the orthogonal array; a separation of 10 mm only diminishes the field generated by the orthogonal array at 5 mm by $\sim 11\%$, and the compromise at 50 mm is even less (figure 19(a)). Interestingly, the force at 5 mm, displayed in figure 19(b), increases for both arrays for larger d , a consequence of the fact that the field gradient in this region is changing more rapidly due to a faster decay in field. At $z = 50 \text{ mm}$, F generated by the diagonal array decays so rapidly with d that, for separations greater than 6 mm, the orthogonal array produces a greater total force than the

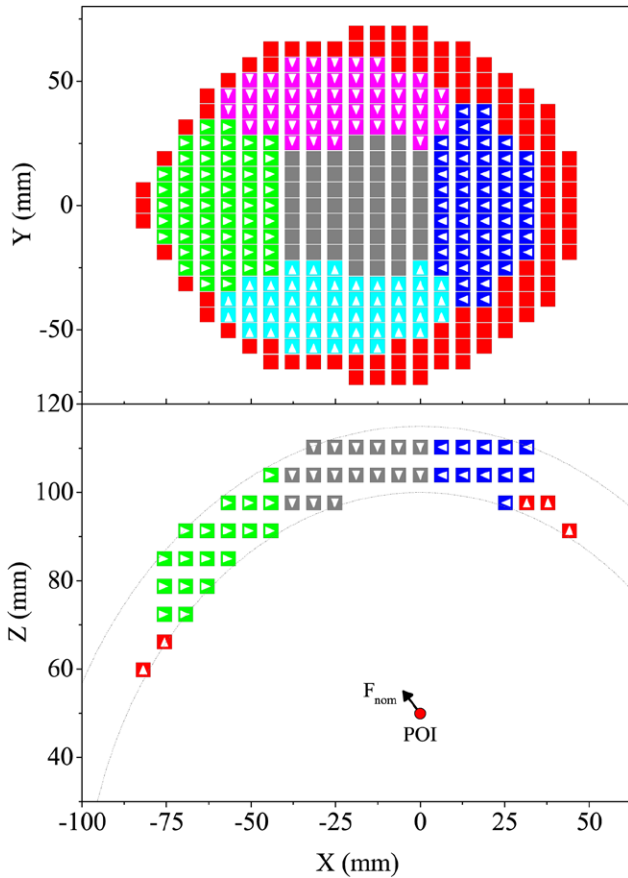


Figure 20. Vector maps displaying the optimized design of a helmet-shaped Halbach array. A view from above, looking down onto the top surface projected on a x - y plane (top), and a side view of the cross-section in the x - z plane (bottom) are shown. The red dot indicates the POI in the x - z plane (50mm from the inside surface of the magnet, on the z -axis), while the black arrow gives the nominal direction of force, 45° to the z -axis. The gray lines show the constraints of the design volume.

diagonal array. This is notable because no other parameter set investigated in the present study yields an optimized arrangement from the orthogonal magnetization set that is capable of applying more force than the analogous design using the diagonal magnetization set.

3.6. Example application

The optimization routine can readily be adapted for specific magnetic drug targeting applications by defining parameters related to the position of interest, nominal direction of force and volume of magnetic material, and also the dimensions of the constrained shape of the optimization volume, taking into account the anatomy and physiology (in particular, fluid flow and vessel diameter in the vessel network near the target) of the targeted region. A design volume was set up to optimize a Halbach array of orthogonally magnetized segments to target and retain magnetic microparticles in the vessel network around the brain at a depth of 50mm, which has a range of possible applications (for example, magnetic microbubbles can be used for localized opening of the blood-brain barrier to deliver drugs to brain tumours [26]). The helmet-shaped

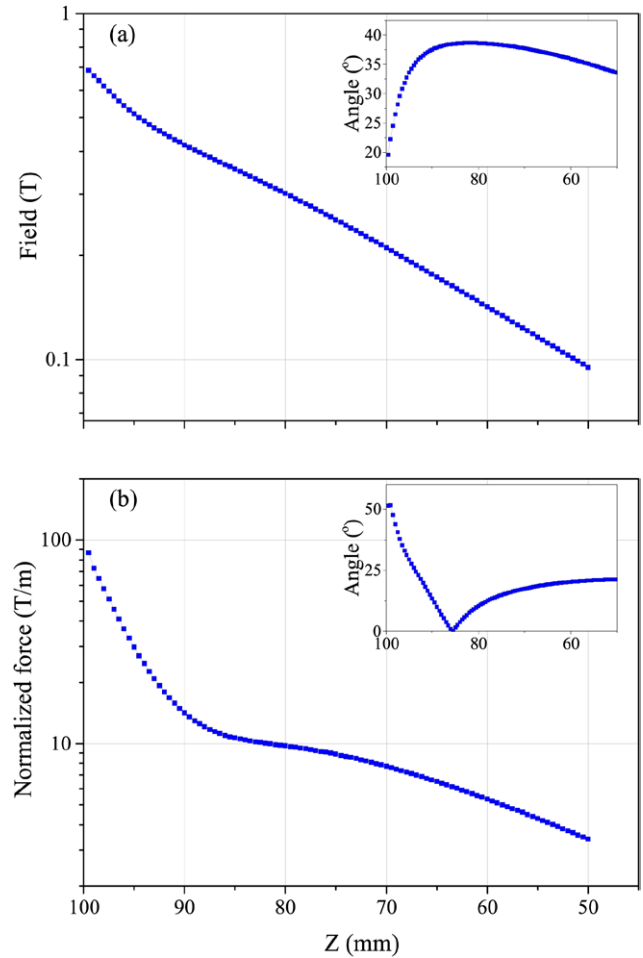


Figure 21. The magnitude of (a) field and (b) normalized force emitted by the optimized helmet-shaped Halbach array along the z -axis, directly below the inside surface of the magnet. (The position axis is plotted so that the source of field is to the left side of the graph for consistency.) The insets show the angle of the relevant vectors with respect to the z -axis, following the conventions described for figure 13.

design volume consisted of a hemisphere with an internal radius of 100mm and a thickness of 15mm above the x - y plane, and the magnet volume was constrained to 200 cc (equivalent to a magnet weight of 1.5kg). The direction of force was set at 45° to the z -axis, to provide a component of force that acts against the general direction of blood flow in the region of interest, along with the component of force that pulls towards the magnet.

The resultant design is shown in figure 20. The top view is similar to the designs of orthogonally magnetized arrays discussed in previous sections, skewed to be more weighted towards the $-x$ quadrants to accommodate the diagonal direction of force. The performance of the array along the z -axis is exhibited in figure 21. Past about 25mm from the inside surface of the magnet, the direction of field and force varies little while the magnitude of these vectors decays approximately exponentially. However, notably the field decays approximately linearly in a region between ~ 15 and 25mm from the magnet, resulting in a relatively consistent magnitude of force over this range. This region also coincides with a transition in the direction of force, with the magnet pulling

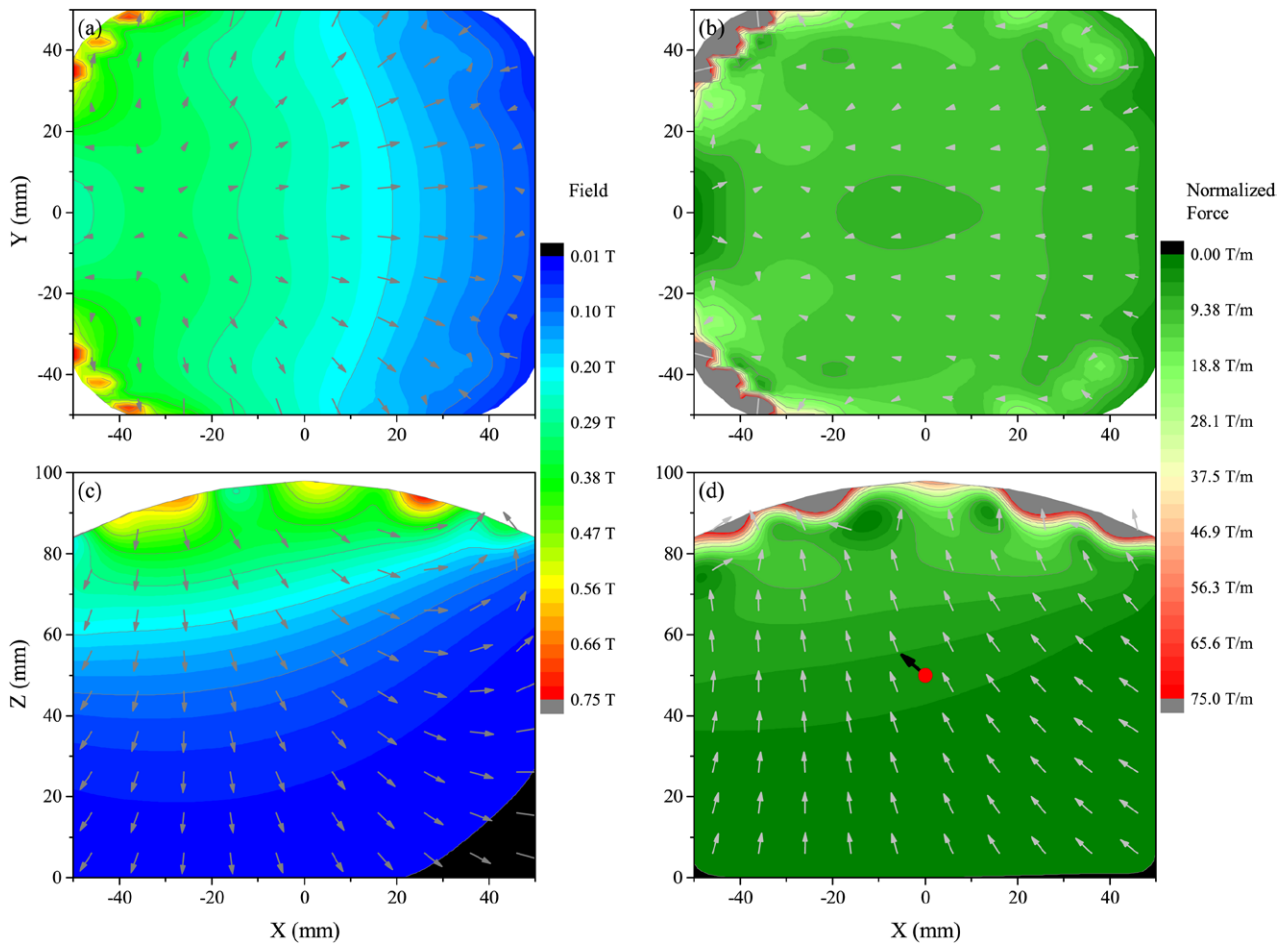


Figure 22. (a) and (b) display the field and force respectively, applied by the helmet-shaped Halbach array in an x - y plane 25 mm below the inside surface of the magnet ($z = 75$ mm). (c) and (d) show the same quantities in the x - z plane below the array. The red dot in (d) indicates the position of interest, while the black arrow displays the nominal direction of force.

in the positive x -direction when $z < 15$ mm (as opposed to the negative x -direction, commensurate with the nominal direction of force, past this transition point). This spatial range is of interest as it approximately corresponds to the depth of the cerebral cortex, which contains vessel diameters typically between 2.5 and 40 micron [55, 56], with flow velocities in the order of ~ 0.5 – 1 mm s^{-1} [48, 49]. Considering a normalized force of ~ 10 T m^{-1} , and extrapolating from the simulations in section 3.4, an extremely high capture efficiency would be expected.

The field and force maps exhibited in figure 22 show that the most intense fields occur near to regions where the magnetization changes between segments in the array. Notably, the nominal direction of force shown in figure 22(d) points from the position of interest, towards the interface between the segments magnetized in the z -direction and the positive x -direction (gray and green segments respectively in figure 20). The change in direction in the force vector seen along the z -axis in figure 21(b) may then be understood as particles getting close enough to the magnet that they are more attracted to the local maximum in field adjacent to the interface between segments magnetized in the z - and negative x -directions (colour-coded gray and blue).

4. Conclusion

An optimization routine developed previously for the design of Halbach arrays consisting of cubic elements has been modified and expanded to generate arbitrarily shaped magnet arrays optimized to deliver magnetic force depending on a range of different design parameters. We have presented designs of optimized uniform magnet geometries and Halbach arrays, demonstrating how the performance of different arrangements varies as a function of the design parameters. The magnetic force applied by the arrays increases logarithmically with magnet volume, while the force emitted at the position of interest decreases almost exponentially as the position of interest gets further from the magnet. The number of allowed magnetization vectors is considered as a design parameter, and while using a greater variety of different magnetizations results in increased force output, it also leads to arrays that are more difficult to assemble, owing to repulsive dipole forces between neighbouring elements. A method to overcome this problem is considered, with simulations suggesting that introducing a small gap between repulsive segments can make optimized Halbach arrays significantly easier to assemble without causing a large compromise to the applied field and force.

Simulations of magnetic microbeads under the influence of fluid flow in a 3 mm wide channel and a subset of optimized array designs performed using COMSOL software suggest that a useful proportion of particles could be captured and retained at short range (5 mm) in mean fluid velocities of 100 mm s⁻¹ or at further depths of 50 mm, when the velocity was 2.5 mm s⁻¹, depending on the choice of magnet. Finally, a design for a helmet magnet to apply an optimal magnetic force 50 mm deep inside the brain was generated to show the versatility of the optimization routine to address specific applications. For this design, particles tend to be most strongly attracted towards regions of the magnet where an interface exists between magnet segments. Based on the flow regime in the cerebral cortex, we suggest a high proportion of trapping in this region is feasible. Our examples of optimized arrays show that, using the present optimization routine, magnet arrays can be designed and assessed for specific magnetic drug targeting applications once the required depth of targeting, direction of magnetic force, volume of magnet and the physiological features and flow regimes around the target have been accounted for.

Acknowledgments

The authors are grateful to the Engineering and Physical Sciences Research Council for supporting the work through grant EP/I021795/1. All data and methods are reported within this paper and at doi:[10.5287/bodleian:RDnk4Aj0k](https://doi.org/10.5287/bodleian:RDnk4Aj0k).

References

- [1] Lübke A S *et al* 1996 Clinical experiences with magnetic drug targeting: a phase i study with 4?-epidoxorubicin in 14 patients with advanced solid tumors *Cancer Res.* **56** 4686–93
- [2] Alexiou C, Arnold W, Klein R J, Parak F G, Hulin P, Bergemann C, Erhardt W, Wagenpfeil S and Lübke A S 2000 Locoregional cancer treatment with magnetic drug targeting *Cancer Res.* **60** 6641–8
- [3] Lübke A S, Alexiou C and Bergemann C 2001 Clinical applications of magnetic drug targeting *J. Surg. Res.* **95** 200–6
- [4] Nobuto H, Sugita T, Kubo T, Shimose S, Yasunaga Y, Murakami T and Ochi M 2004 Evaluation of systemic chemotherapy with magnetic liposomal doxorubicin and a dipole external electromagnet *Int. J. Cancer* **109** 627–35
- [5] Dandamudi S and Campbell R B 2007 The drug loading, cytotoxicity and tumor vascular targeting characteristics of magnetite in magnetic drug targeting *Biomaterials* **28** 4673–83
- [6] Kyrtatos P G, Lehtolainen P, Junemann-Ramirez M, Garcia-Prieto A, Price A N, Martin J F, Gadian D G, Pankhurst Q A and Lythgoe M F 2009 Magnetic tagging increases delivery of circulating progenitors in vascular injury *JACC: Cardiovasc. Interventions* **2** 794–802
- [7] Chen J, Huang N, Ma B, Maitz M F, Wang J, Li J, Li Q, Zhao Y, Xiong K and Liu X 2013 Guidance of stem cells to a target destination *in vivo* by magnetic nanoparticles in a magnetic field *ACS Appl. Mater. Interfaces* **5** 5976–85
- [8] Gao Y, Lim J, Teoh S-H and Xu C 2015 Emerging translational research on magnetic nanoparticles for regenerative medicine *Chem. Soc. Rev.* **44** 6306–29
- [9] Pankhurst Q A, Connolly J, Jones S K and Dobson J 2003 Applications of magnetic nanoparticles in biomedicine *J. Phys. D: Appl. Phys.* **36** R167
- [10] Kozissnik B and Dobson J 2013 Biomedical applications of mesoscale magnetic particles *MRS Bull.* **38** 927–32
- [11] Shapiro B, Kulkarni S, Nacev A, Muro S, Stepanov P Y and Weinberg I N 2015 Open challenges in magnetic drug targeting *Wiley Interdiscip. Rev.: Nanomed. Nanobiotechnol.* **7** 446–57
- [12] Forbes Z G, Yellen B B, Barbee K A and Friedman G 2003 An approach to targeted drug delivery based on uniform magnetic fields *IEEE Trans. Magn.* **39** 3372–7
- [13] Grief A D and Richardson G 2005 Mathematical modelling of magnetically targeted drug delivery *J. Magn. Magn. Mater.* **293** 455–63 (*Proc. of the 5th Int. Conf. on Scientific and Clinical Applications of Magnetic Carriers*)
- [14] Häfeli U O, Gilmour K, Zhou A, Lee S and Hayden M E 2007 Modeling of magnetic bandages for drug targeting: button versus halbach arrays *J. Magn. Magn. Mater.* **311** 323–9 (*Proc. of the 6th Int. Conf. on the Scientific and Clinical Applications of Magnetic Carriers*)
- [15] Driscoll C F, Morris R M, Senyei A E, Widder K J and Heller G S 1984 Magnetic targeting of microspheres in blood flow *Microvascular Res.* **27** 353–69
- [16] Mathieu J-B, Beaudoin G and Martel S 2006 Method of propulsion of a ferromagnetic core in the cardiovascular system through magnetic gradients generated by an mri system *IEEE Trans. Biomed. Eng.* **53** 292–9
- [17] Cao Q, Han X and Li L 2012 Numerical analysis of magnetic nanoparticle transport in microfluidic systems under the influence of permanent magnets *J. Phys. D: Appl. Phys.* **45** 465001
- [18] Owen J, Grove P, Rademeyer P and Stride E 2014 The influence of blood on targeted microbubbles *J. R. Soc. Interface* **11** 20140622
- [19] Pankhurst Q A, Thanh N T K, Jones S K and Dobson J 2009 Progress in applications of magnetic nanoparticles in biomedicine *J. Phys. D: Appl. Phys.* **42** 224001
- [20] Stride E, Porter C, Prieto A G and Pankhurst Q 2009 Enhancement of microbubble mediated gene delivery by simultaneous exposure to ultrasonic and magnetic fields *Ultrasound Med. Biol.* **35** 861–8
- [21] Pouponneau P, Leroux J-C and Martel S 2009 Magnetic nanoparticles encapsulated into biodegradable microparticles steered with an upgraded magnetic resonance imaging system for tumor chemoembolization *Biomaterials* **30** 6327–32
- [22] Pouponneau P, Leroux J-C, Soulez G, Gaboury L and Martel S 2011 Co-encapsulation of magnetic nanoparticles and doxorubicin into biodegradable microcarriers for deep tissue targeting by vascular MRI navigation *Biomaterials* **32** 3481–6
- [23] Aadinath W, Ghosh T and Anandharamkrishnan C 2016 Multimodal magnetic nano-carriers for cancer treatment: challenges and advancements *J. Magn. Magn. Mater.* **401** 1159–72
- [24] Wadajkar A S, Bhavsar Z, Ko C-Y, Koppolu B, Cui W, Tang L and Nguyen K T 2012 Multifunctional particles for melanoma-targeted drug delivery *Acta Biomaterialia* **8** 2996–3004
- [25] Schleich N, Po C, Jacobs D, Ucakar B, Gallez B, Danhier F and Préat V 2014 Comparison of active, passive and magnetic targeting to tumors of multifunctional paclitaxel/spio-loaded nanoparticles for tumor imaging and therapy *J. Control. Release* **194** 82–91
- [26] Fan C-H, Ting C-Y, Lin H-J, Wang C-H, Liu H-L, Yen T-C and Yeh C-K 2013 Spio-conjugated, doxorubicin-loaded microbubbles for concurrent MRI and focused-ultrasound enhanced brain-tumor drug delivery *Biomaterials* **34** 3706–15

- [27] Zhang X, Chen F and Ni J 2009 A novel method to prepare magnetite chitosan microspheres conjugated with methotrexate (mtx) for the controlled release of mtx as a magnetic targeting drug delivery system *Drug Delivery* **16** 280–8
- [28] Hu Y, Liu C, Li D, Long Y, Song K and Tung C-H 2015 Magnetic compression of polyelectrolyte microcapsules for controlled release *Langmuir* **31** 11195–9
- [29] Bi F, Zhang J, Su Y, Tang Y-C and Liu J-N 2009 Chemical conjugation of urokinase to magnetic nanoparticles for targeted thrombolysis *Biomaterials* **30** 5125–30
- [30] Mangual J O, Li S, Ploehn H J, Ebner A D and Ritter J A 2010 Biodegradable nanocomposite magnetite stent for implant-assisted magnetic drug targeting *J. Magn. Magn. Mater.* **322** 3094–100
- [31] Hatch G P and Stelter R E 2001 Magnetic design considerations for devices and particles used for biological high-gradient magnetic separation (hgms) systems *J. Magn. Magn. Mater.* **225** 262–76 (*Proc. of the 3rd Int. Conf. on Scientific and Clinical Applications of Magnetic Carriers*)
- [32] Rotariu O and Strachan N J C 2005 Modelling magnetic carrier particle targeting in the tumor microvasculature for cancer treatment *J. Magn. Magn. Mater.* **293** 639–46 (*Proc. of the 5th Int. Conf. on Scientific and Clinical Applications of Magnetic Carriers*)
- [33] Hayden M E and Häfeli U O 2006 ‘Magnetic bandages’ for targeted delivery of therapeutic agents *J. Phys.: Condens. Matter* **18** S2877
- [34] Cao Q, Han X and Li L 2011 Enhancement of the efficiency of magnetic targeting for drug delivery: development and evaluation of magnet system *J. Magn. Magn. Mater.* **323** 1919–24
- [35] Nacev A, Komaee A, Sarwar A, Probst R, Kim S H, Emmert-Buck M and Shapiro B 2012 Towards control of magnetic fluids in patients: directing therapeutic nanoparticles to disease locations *IEEE Control Syst.* **32** 32–74
- [36] Sarwar A, Nemirovski A and Shapiro B 2012 Optimal halbach permanent magnet designs for maximally pulling and pushing nanoparticles *J. Magn. Magn. Mater.* **324** 742–54
- [37] Barnsley L C, Carugo D, Owen J and Stride E 2015 Halbach arrays consisting of cubic elements optimised for high field gradients in magnetic drug targeting applications *Phys. Med. Biol.* **60** 8303
- [38] Alexiou C, Diehl D, Henninger P, Iro H, Rockelein R, Schmidt W and Weber H 2006 A high field gradient magnet for magnetic drug targeting *IEEE Trans. Appl. Supercond.* **16** 1527–30
- [39] Bean C P and Livingston J D 1959 Superparamagnetism *J. Appl. Phys.* **30** S120–9
- [40] Williams H D, O’Grady K, El Hilo M and Chantrell R W 1993 Superparamagnetism in fine particle dispersions *J. Magn. Magn. Mater.* **122** 129–33
- [41] Majetich S A, Scott J H, Kirkpatrick E M, Chowdary K, Gallagher K and McHenry M E 1997 Magnetic nanoparticles and magnetocrystalline anisotropy *Nanostruct. Mater.* **9** 291–300
- [42] Kayal S, Bandyopadhyay D, Mandal T K and Ramanujan R V 2011 The flow of magnetic nanoparticles in magnetic drug targeting *RSC Adv.* **1** 238–46
- [43] Takeda S, Mishima F, Fujimoto S, Izumi Y and Nishijima S 2007 Development of magnetically targeted drug delivery system using superconducting magnet *J. Magn. Magn. Mater.* **311** 367–71 (*Proc. of the 6th Int. Conf. on the Scientific and Clinical Applications of Magnetic Carriers*)
- [44] Mishima F, Takeda S-I, Izumi Y and Nishijima S 2007 Development of magnetic field control for magnetically targeted drug delivery system using a superconducting magnet *IEEE Trans. Appl. Supercond.* **17** 2303–6
- [45] Sarwar A, Lee R, Depireux D A and Shapiro B 2013 Magnetic injection of nanoparticles into rat inner ears at a human head working distance *IEEE Trans. Magn.* **49** 440–52
- [46] Shapiro B, Kulkarni S, Nacev A, Sarwar A, Preciado D and Depireux D A 2014 Shaping magnetic fields to direct therapy to ears and eyes *Annu. Rev. Biomed. Eng.* **16** 455–81
- [47] Fukui S, Abe R, Ogawa J, Oka T, Yamaguchi M, Sato T and Imaizumi H 2007 Study on optimization design of superconducting magnet for magnetic force assisted drug delivery system *Physica C* **463–5** 1315–8 (*Proc. of the 19th Int. Symp. on Superconductivity*)
- [48] Villringer A, Them A, Lindauer U, Einh K and Dirnagl U 1994 Capillary perfusion of the rat brain cortex. An *in vivo* confocal microscopy study *Circ. Res.* **75** 55–62
- [49] Lorthois S, Cassot F and Lauwers F 2011 Simulation study of brain blood flow regulation by intra-cortical arterioles in an anatomically accurate large human vascular network. Part II: flow variations induced by global or localized modifications of arteriolar diameters *NeuroImage* **54** 2840–53
- [50] Shimamoto K, Sakuma S, Ishigaki T and Makino N 1987 Intratumoral blood flow: evaluation with color doppler echography *Radiology* **165** 683–5
- [51] Taylor A, Jurkovic D, Bourne T H, Natucci M, Collins W P and Campbell S 1996 A comparison of intratumoural indices of blood flow velocity and impedance for the diagnosis of ovarian cancer *Ultrasound Med. Biol.* **22** 837–43
- [52] Owen J, Rademeyer P, Chung D, Cheng Q, Holroyd D, Coussios C, Friend P, Pankhurst Q A and Stride E 2015 Magnetic targeting of microbubbles against physiologically relevant flow conditions *Interface Focus* **5** 20150001
- [53] Lee J Y, Carugo D, Crake C, Owen J, de Saint Victor M, Seth A, Coussios C and Stride E 2015 Nanoparticle-loaded protein-polymer nanodroplets for improved stability and conversion efficiency in ultrasound imaging and drug delivery *Adv. Mater.* **27** 5484–92
- [54] Cugat O, Byrne R, McCaulay J and Coey J M D 1994 A compact vibrating sample magnetometer with variable permanent magnet flux source *Rev. Sci. Instrum.* **65** 3570–3
- [55] Cassot F, Lauwers F, Fouard C, Prohaska S and Lauwers-Cances V 2006 A novel three-dimensional computer-assisted method for a quantitative study of microvascular networks of the human cerebral cortex *Microcirculation* **13** 1–18
- [56] Lorthois S, Cassot F and Lauwers F 2011 Simulation study of brain blood flow regulation by intra-cortical arterioles in an anatomically accurate large human vascular network. Part I: methodology and baseline flow *NeuroImage* **54** 1031–42